Geoscientific
Model Development
Discussions

1 IITM High-Resolution Global Forecast Model Version 1: An attempt

2 to resolve monsoon prediction deadlock

3 R. Phani Murali Krishna[1], Siddharth Kumar[1], A. Gopinathan Prajeesh[2], Peter Bechtold[3], Nils Wedi[3],

4 Kumar Roy[4], Malay Ganai[1], B. Revanth Reddy[1], Snehlata Tirkey[1], Tanmoy Goswami[1] , Radhika

5 Kanase[1], and Parthasarathi Mukhopadhyay[1]

6

7 [1]Indian Institute of Tropical Meteorology, Ministry of Earth Sciences, Dr. Homi Bhabha Road, Pune 411008, India
8 [2] King Abdullah University of Science and Technology, Saudi Arabia
9 [3] ECMWF
10 [4] University of Victoria, Canada
11

12

13

14 *Correspondence to*: Dr. P. Mukhopadhyay (mpartha@tropmet.res.in; parthasarathi64@gmail.com)

15

16

17

18

19

20

21

22

23

24

25

26 **Abstract.** The prediction of Indian monsoon rainfall variability affecting a country with a population of billions remained
27 one of the major challenges of the numerical weather prediction community. While in recent years, there has been a
28 significant improvement in predicting the synoptic scale transients associated with the monsoon circulation, the intricacies of
29 rainfall variability remained a challenge. Here, an attempt is made to develop a global model using a dynamic core of a cubic
30 octahedral grid that provides a higher resolution of 6.5 km over the global tropics. This high-resolution model has been
31 developed to resolve the monsoon convection. Reforecasts with the IITM High-resolution Global Forecast Model (HGFM)
32 have been run daily from June through September 2022. The HGFM model has a wave number truncation of 1534 in the
33 cubic octahedral grid. The monsoon events have been predicted with a ten-day lead time. The HGFM model is compared to
34 the operational GFS T1534. While the HGFM provides skills comparable to the GFS, it shows better skills for higher
35 precipitation thresholds. This model is currently being run in experimental mode and will be made operational.

36
37
38
39
40
41
42
43
44
45
46
47
48
49
50
51
52
53
54
55
56
57

1 Introduction

In spite of significant improvement in numerical weather prediction skill in the last decades (Bechtold et al., 2008; Magnusson and Kallen 2013; Hoffman et al., 2018) predictions of tropical rainfall variability remain a challenge (Westra et al., 2014; Prakash et al., 2016). Stephens et al. (2010) demonstrated that the models predict in the tropics too many rainy days which are in the lighter rain category. The challenges of tropical rainfall variability have also been demonstrated by Watson et al., 2017. The vagaries of the Indian monsoon every year affect the lifestyle of billions of people and the economy of the Indian sub-continent modulating its Gross Domestic Product (GDP) (Gadgil and Gadgil, 2006). It is therefore of the utmost importance to improve the weather prediction skill in general and extreme precipitation events in particular. With the increase of computing power, the resolution of numerical weather prediction models have been increasing and global models with a resolution of 1~7 km have become a reality (Miura et al., 2007; Satoh et al., 2005; Satoh et al., 2019; Wedi et al., 2020). The higher resolution of Numerical Weather Prediction (NWP) models has been found to produce a realistic rainfall variability across scales including diurnal variation, better Madden Julian Oscillation (MJO) variability and seasonal mean climate (Kinter et al., 2013; Rajendran and Kitoh, 2008; Skamarock et al., 2012; Molod et al., 2015; Crueger et al. 2018; Giorgetta et al., 2018). In India, operational NWP was initiated with moderate resolution of T80 and then gradually enhanced to T382, T574 (Prasad et al., 2011, 2014, 2017) and very recently to T1534 (Mukhopadhyay et al., 2019). The advantage of using higher resolution (T1534~12.5 km) as against the lower resolution T574 (~27 km) was found by enhancement of the model skill by 2 days (Rao et al., 2019). The National Centre for Environmental Prediction (NCEP) GFS model with 21 members has been used for probabilistic forecasts since June 2018 (Deshpande et al., 2021). The high-resolution GFS T1534 is found to enhance the skill of heavy rainfall event (Mukhopadhyay et al., 2019), tropical cyclones and even block level prediction of rainfall (block is a sub-division of a districts in India, typically of the size of the grid of GFS T1534). However, the skill of the GFS T1534 for prediction of extremely heavy precipitation can still be improved particularly over the orographic regions of India such as the southern coastal state of Kerala, India (Mukhopadhyay et al., 2021).

The 12-km deterministic and the ensemble model based on the GFS do show reasonably good skill in capturing the monsoon rainfall with 3 to 5 days lead time. The skill of the GFS forecast for Indian monsoon has been reported by Mukhopadhyay et al. (2019) and the skill of tropical cyclones with the Global Ensemble Forecast System (GEFS) has also been reported in Deshpande et al. (2021). However, in a recent study Mukhopadhyay et al. (2021) showed that three state-of-the-art ensemble forecast systems namely the GEFS, the United Kingdom Meteorological Office (UKMO) based NCMRWF Ensemble Prediction System (NEPS) run by National Centre for Medium Range Weather Forecasting (NCMRWF) and the Integrated Forecasting System (IFS) by ECMWF struggled to capture the extremely heavy rainfall over Kerala state of India during August 2018 and August 2019 extremely heavy rainfall episode. This in fact brought up the limitation of the model in resolving the rainfall variability over the Indian region and more importantly over the orographic region. One of the limitations in resolving the regional variabilities of rainfall is the horizontal resolution which does not allow the model to resolve the smaller scale processes. Therefore, a need was felt to enhance the horizontal resolution of the existing GFS based

91   forecasting system. As running of a model close to the convection permitting model (at a resolution lesser than 10 km) is

92   computationally too expensive in conventional linear reduced Gaussian grids, it was thought to build a weather model with a

93   grid which has a variable resolution from the pole to the equator. In view of this, the Tco has been identified and the GFS

94   linear reduced Gaussian Grid at triangular truncation 1534 is replaced by an equivalent truncation of 1534 in cubic

95   octahedral grid. The equivalent model resolutions of the linear Tl1534 and the cubic Tco1543 grids are displayed in Fig. 1a.

96   Indeed, as the linear grid has a roughly uniform grid point resolution of 12.5 km the octahedral grid has a resolution of about

97   8 km in the Polar Regions and around 6 km in the tropical band. One of the prominent examples of the Global NWP model

98   with the Tco grid is that of the European Centre for Medium-Range Weather Forecasts (ECMWF) model suites. The Tco

99   grid provides several advantages (ECMWF Documentation Cy43r1, 2016) over that of the conventional reduced Gaussian

100   linear grid (Fig. 1a), to name a few- significant reduction in computation cost, improved representation of orography, better

101   filtering and better conservation properties. These properties of Tco make it a better candidate, particularly for the utilization

102   of high-performance computers (HPC).

103   This paper is the first attempt to best of our knowledge, towards building a model close to a convection permitting global

104   weather model in India with an emphasis to Indian monsoon rainfall variability. The details of the model development and

105   the experiments conducted have been elaborated in Sect. 2. The model results are analysed in Sect. 3, and the conclusion of

106   the study is summarized in Sect. 4.

2 Model, Data and Methodology

108   This A new grid, namely the Triangular Cubic Octahedral (Tco) grid, has been adopted to change the existing GFS (semi-

109   lagrangian) Gaussian linear model system. In the spectral domain, dynamical fields are represented by the sum of spherical

110   harmonics. The total wavenumber characterizes the spherical harmonics, and the associated wavelength is the ratio of the

111   circumference of the Earth to the total wavenumber. The value of the maximum wavenumber (n_max) used to represent a

112   field as the sum of spherical harmonics is also the spectral truncation of the model. In the case of both GFS and Tco, the

113   value of n_max is 1534. For the same spectral truncation n_max, the number of latitude circles from the equator to the pole

114   can vary depending on the choice of spectral transformation. For a linear grid, n_max=2N-1, and for a cubic grid, n_max=N-

115   1. Therefore, for a linear Gaussian grid, the smallest wavelength is represented by only two grid points, as is the case with

116   the GFS 1534 model. However, in the case of triangular truncation, the smallest wavelength is represented by four grid

117   points (in the case of the Tco grid). In triangular truncation, for the same spectral truncation, the number of latitude circles is

118   about double that of the linear truncation. For the GFS model, the horizontal resolution is ~12.5 km, and applying the cubic

119   grid ensures that the horizontal resolution becomes ~6.5 km in the tropics (about half of the currently used model resolution)

120   for the Tco grid. In the Tco grid, the number of latitude circles is 1535.

121   Once a particular choice of spectral truncation is made, the number of latitude circles becomes obvious. However, the

122   number of longitude circles per latitude circle remains to be prescribed for the creation of the global grid structure. In a fully

4

123 Gaussian grid, the number of longitude circles per latitude circle remains the same throughout the latitudes from the equator
124 to the pole. Thus, the effective resolution near the poles becomes very high compared to the equatorial regions. This specific
125 requirement demands too many computational resources and poses problems of numerical instability. To overcome that, in
126 the linear Gaussian grid, the number of latitude circles decreases in a certain way from the equator toward the pole to ensure
127 almost the same zonal resolution. For the cubic octahedral grid, the number of longitude points per latitude circle is
128 prescribed in a different way. The latitude circle closest to the pole consists of 20 longitude points, and the number of
129 longitude points increases by 4 at each latitude circle, moving from poles towards the equator. The number of longitude
130 points at the equator in the case of the Tco grid is given by $Nx=20+1534*4=6156$. Therefore, the zonal grid
131 length$=2pi*R/Nx\sim6.5$ km. In the original reduced Gaussian grid, the number of longitude points per latitude remains fixed in
132 different blocks of latitudes. The number of latitude points jumps from one block to the other by a constant number. Unlike
133 the linear reduced Gaussian grid, the horizontal resolution varies more smoothly with latitudes in Tco. The Collignon
134 projection of a sphere obtains this configuration onto an octahedron. In the current study, the Tco grid at truncation
135 wavenumber of 1534 is being used. Fig. 1a and Fig. 1b depicts the variation of grid resolution with latitude in the GFS (SL)
136 and HGFM (Tco).

137 Before testing the HGFM with complete physics (see Table 1 for description of physics being used in both versions of
138 model), we have made a version of HGFM with only a dynamical core following Held and Suarez (1994), referred to as
139 HS94. The HS94 is run to check the stability of the Tco grid framework. Surface boundary conditions for the Tco grid have
140 been meticulously prepared to ensure the accuracy of grid-point representation. Moreover, the HGFM (Tco1534) has been
141 developed with complete physics and incorporates essential boundary conditions, including global topography, global land-
142 use-land-cover etc. The HGFM at Tco1534 truncation is depicted over the globe in Fig. 1. The model has been run daily for
143 a ten days forecast at IITM Pratyush HPC system. To understand the computational efficiency of Tco model, time taken for
144 one day forecast is compared for GFS 1534 and HGFM model (Tco 765 in this case) (see Fig. 1c). A comparison between
145 GFS 1534 and Tco 765 is made because both models have almost same number of grid points. It is clear that Tco 765
146 significantly saves the runtime in dynamical core and total time as well. Moreover, Tco model is in general more scalable for
147 higher number of cores (not shown). The model has been run for the summer monsoon season of June, July, August and
148 September (JJAS) 2022. A detailed analysis of the model run has been discussed in the results section. Apart from the
149 monsoon season, few case studies have also been discussed.

Geoscientific
Model Development
Discussions

150
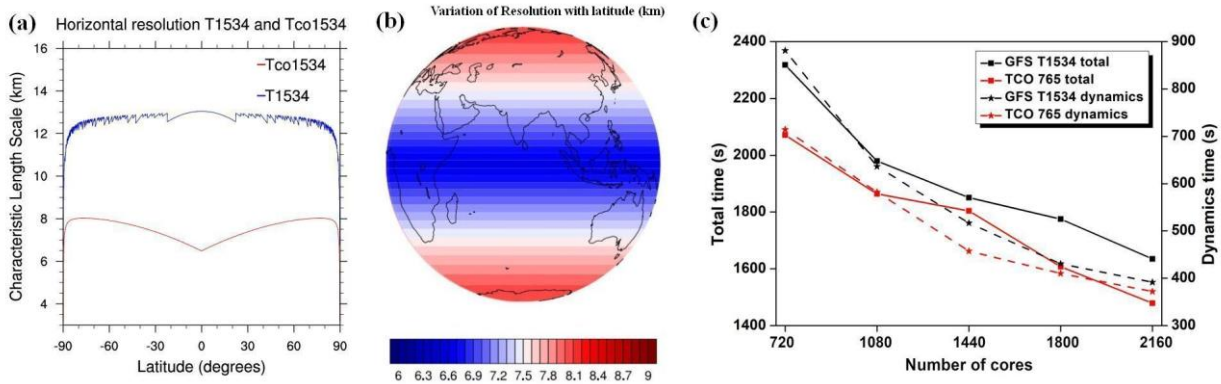
Figure 1. Variation of grid length with latitude in GFS (blue) and Tco (red) (a), depiction of grid resolution over the globe in Tco grid (b), total and dynamics time taken for different number of cores (c). Time taken by GFS and HGFM for one day forecast (Left vertical axis is total time taken and right axis represents time taken by model dynamics).

To verify the model forecast, the daily observed gridded rainfall data from the Integrated Multi-satellite Retrievals for GPM (IMERG) version 06B (Huffman et al., 2019) rainfall data at 0.1° × 0.1° (10 km) horizontal resolution is utilized for the year of 2022 for JJAS season. Additionally, to validate a heavy rainfall event over India, gridded rainfall from India Meteorological Department (IMD) at 25 km resolution is used. The IMD rainfall data are merged product of gridded rain gauge observations and GPM satellite-estimated rainfall over the ISM region (Mitra et al., 2014). Further, the reanalysis-based parameters from the fifth generation of ECMWF atmospheric reanalyses (ERA5) products (Hersbach and Dee, 2016) are utilized at 25 km horizontal resolution during JJAS of the year 2022.

Table 1. Details of domain configuration and physics options used in HGFM.

| Physics	Description
Radiation	Rapid Radiative Transfer Model (RRTM) for both Shortwave and Longwave (Iacono et al., 2000; Clough et al., 2005) with Monte Carlo Independent Column Approximation (McICA)
Microphysics	Formulated grid-scale condensation and precipitation (Sundqvist et al., 1989; Zhao and Carr, 1997)
Convection	Aerosol aware and Mass flux based Simplified Arakawa-Schubert (SAS) shallow convection (Pan and Wu, 1995; Han and Pan, 2011; Arakawa and Wu, 2013; Han et al., 2017)
Planetary Boundary Layer (PBL)	Hybrid Eddy-Diffusivity Mass Flux vertical turbulent mixing scheme (Han and Pan, 2011; Han et al., 2016)
Gravity Wave Drag (GWD)	Mountain blocking (Alpert et al., 1988; Kim and Arakawa, 1995; Lott and Miller, 1997) and stationary convective-forced GWD (Chun and Baik, 1998)

162

3 Results and Discussions

3.1 200 hPa Kinetic Energy Spectra

Before going into the details of model validation, the first metric to evaluate the model fidelity is to validate the Kinetic Energy (KE) spectra of 200 hPa wind. The KE spectra provide information about the distribution of kinetic energy across the scale. A close resemblance between observed /reanalysis-based spectra and spectra produced by the model gives confidence about accuracy of overall model configuration. The kinetic energy (KE) spectrum in the upper troposphere exhibits two clearly defined power-law patterns. From observational studies, it is established that at large-scale, rotational modes prevail (k^{-3}) while at mesoscales, divergent modes are dominant ($k^{-5/3}$) (Nastrom and Gage, 1985). Figure 2 shows the KE spectra of 200 hPa wind simulated by HGFM and GFS T1534. The KE spectra for the forecast up to 3 days lead time has been compared with ERA5 data. While both the models reasonably capture $k^{-5/3}$ behaviour of the mesoscale at the higher wavenumber, but the HGFM appears to capture the k^{-3} behaviour of the large scale at the lower wavenumber closer to observation. The KE spectra indicates that overall configuration of both versions of the model is robust. Therefore, now we turn our attention towards verification of convective available potential energy and rainfall simulations, the most desirable parameter in model forecasts.
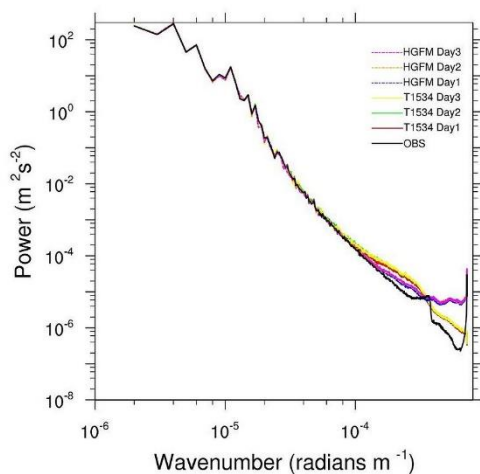
**Figure 2. Kinetic energy spectra of 200 hPa wind for observation and different lead times of GFS T1534 and HGFM.**

3.2 Quasi-equilibrium in models

Both model versions are run at high-resolutions, close to convection-permitting models' resolution. However, in this case, a scale-aware convection scheme is used to parameterize deep convection in the model. From observational studies it has been established that tropical atmosphere deviates significantly from the convective-quasi equilibrium (e.g., Zhang, 2003). The convective quasi-equilibrium (CQE) is the fundamental approach used in most models for parameterization of deep convection (Arakawa and Schubert 1974). To understand up to what extent both model versions obey CQE, we adopted

7

methodology suggested in Kumar et al. (2022). The absolute value of changes in Convective Available Potential Energy (CAPE) at daily timescales is analysed from GFS T1534 and HGFM models for the year 2022 during JJAS and compared with the ERA-5 data (Fig. 3). Notable changes were observed in the daily dCAPE values between GFS T1534 and HGFM compared to ERA-5. The daily dCAPE values from ERA-5 (Fig. 3a, d) data matches better with the HGFM (Fig. 3e, f) than GFS T1534 (Fig. 3b, c) for day 1 and day 3 lead times.
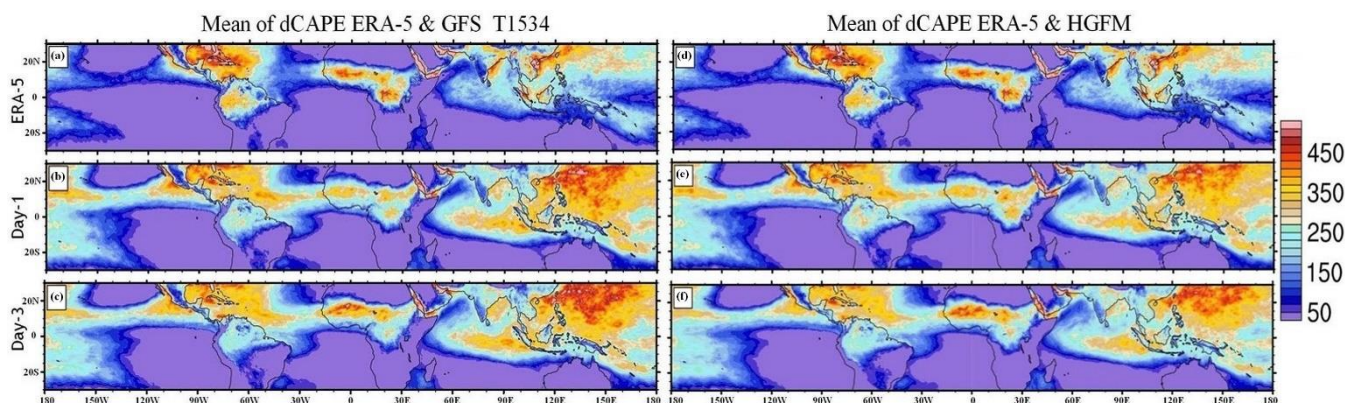

Figure 3. Comparison of dCAPE mean during JJAS 2022 from ERA-5 (a, d) with respect to GFS T1534 (b, c) and TCO 1534 (e, f) for day-1 and day-3 lead time.

3.3 Analysis of Global precipitation

The global precipitation bias of GFS (left panel of Fig. 4 and HGFM (right panel) with respect to Integrated Multi-satellite Retrievals for GPM (IMERG) data, with day 1, day 3 and day 5 lead time is shown in Fig. 4. Both the models broadly show a similar rainfall bias over the global land and global ocean. However, there are some subtle differences. The day 1 forecast (Fig. 4a) of GFS shows a wet bias over the equatorial eastern Pacific extending up to the tropical western Pacific. On the other hand, the HGFM on day 1 lead (Fig. 4d) also shows a wet bias mostly confined over the tropical eastern Pacific and a slight negative bias over western Pacific. For HGFM, the positive bias of rainfall over the tropical ocean appears to be mostly over the eastern Pacific while that of GFS appears to be over eastern Pacific and extending towards the central and west Pacific for all the lead time. Apart from the oceanic region, the major global land regions (central African Continent, Maritime continent, Indian summer monsoon region, northern part of South America) shows a negative bias in both the models at different lead times (Fig. 4) which is likely related to the model physical parameterizations.

Geoscientific
Model Development
Discussions
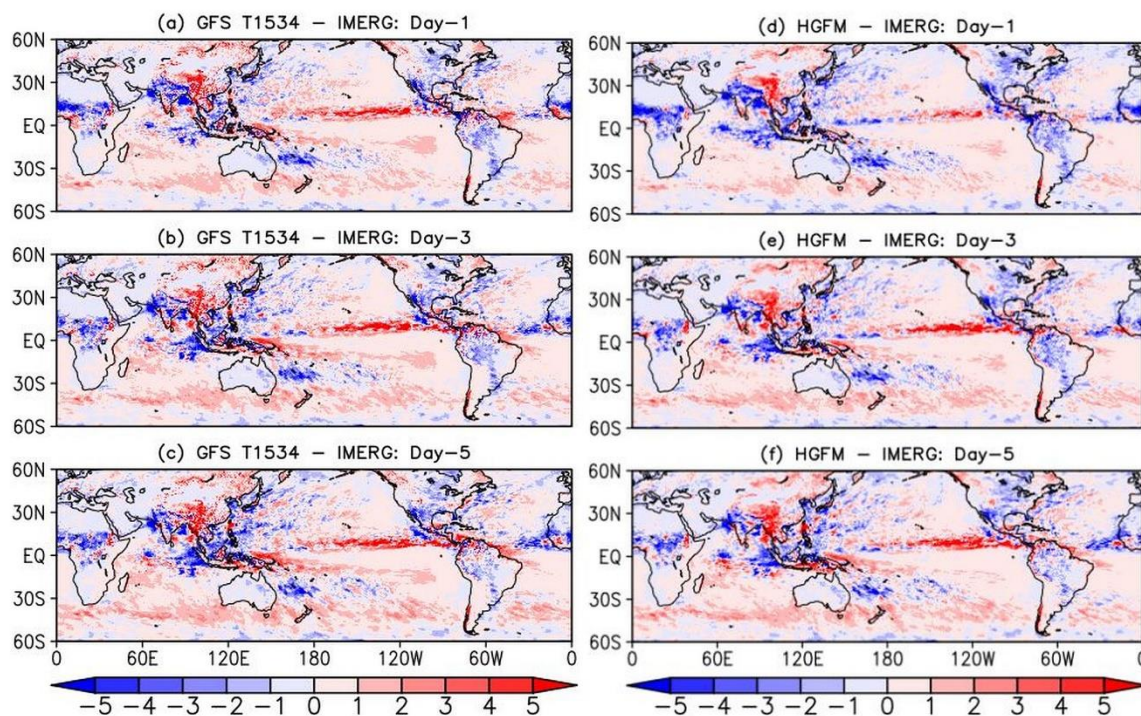
Figure 4. Global JJAS precipitation bias (mm day-1) of GFS T1534 (left panel) with respect to IMERG for (a) day-1, (b) day-3 and (c) day-5 lead time. Right column (d-f) indicates similar plots but for HGFM.

3.4 Indian summer monsoon precipitation and related features

While Fig. 4 depicted the precipitation bias over the global domain, it will be interesting to investigate the model forecast performance over the complex orographic region over the Indian domain, the region of our utmost interest. As mentioned earlier, one of the major advantages of using a Tco grid is a better representation of orography. Therefore, it is imperative to investigate the forecast skill of the high resolution HGFM model over the mountainous Himalayan foothills, adjoining northeast India, and Western Ghats (WGs) region (shown in Fig. 5 and 6 respectively). The GFS T1534 model forecasts indicate spurious rainfall activity over the Himalayan foothills and northeast India region for all lead times (Fig. 5b-d). On contrary, the HGFM model with finer horizontal resolution largely resolves the spurious rainfall over the region as shown in Fig. 5e-g. The Gibbs waves are largely suppressed over the mountainous terrains in HGFM compared to GFS T1534. Similarly, the precipitation distribution over the WGs region shows considerable overestimation in GFS T1534 for all lead times (Fig. 6b-d). On the other hand, the magnitude of overestimation is decreased considerably in HGFM forecasts as depicted in Fig. 6e-g. Thus, the above analysis brings out the fact that HGFM shows its potential in predicting realistic rainfall distribution over the orographic regions.

9

Geoscientific
Model Development
Discussions
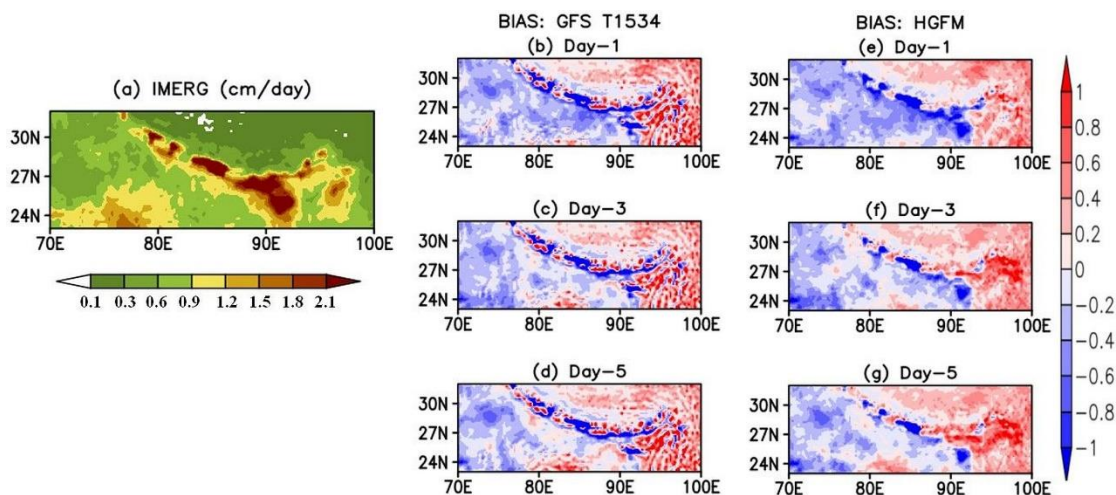
Figure 5. Comparison of JJAS mean precipitation (mm/day) and Bias in IMERG data (cm/day) (a) with GFS T1534 (b, c, d) and TCO 1534 (e, f, g) during 2022 over Himalayan foothills and Northeast India for day-1 day-3 and day-5 lead time.
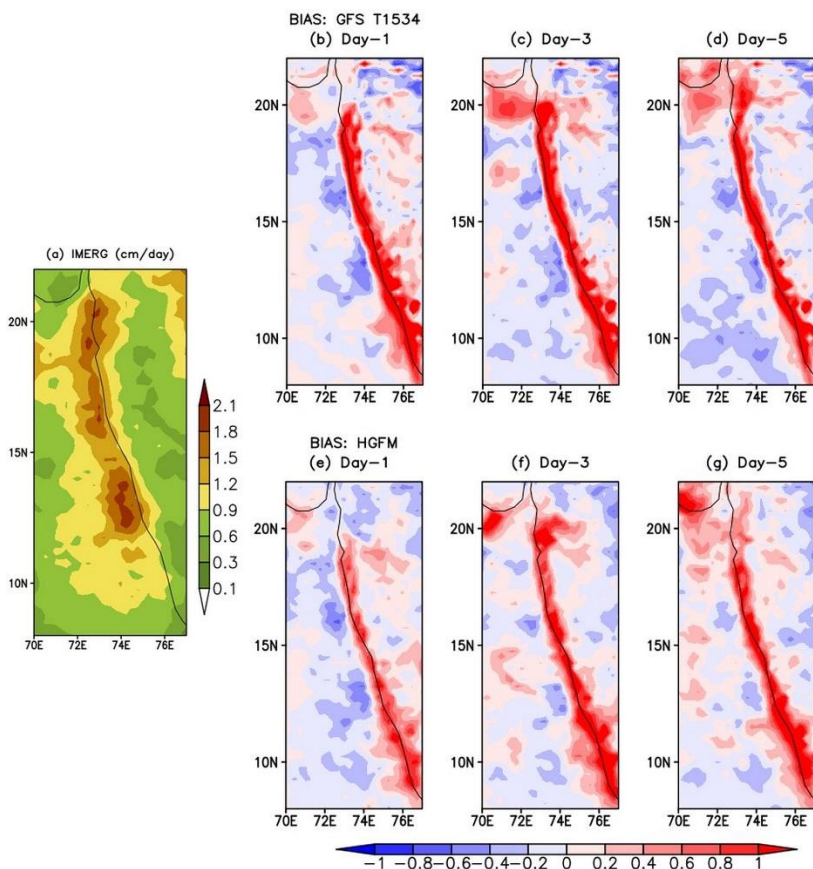

Figure 6. Comparison of JJAS mean precipitation (mm/day) and Bias in IMERG data (cm/day) (a) with GFS T1534 (b, c, d) and TCO 1534 (e, f, g) during 2022 over Western ghats region for day-1 day-3 and day-5 lead time.

226   One of the prominent features of ISM is vertical shear of zonal wind. Previous studies (Jiang et al., 2004; Abhik et al., 2013)
227   demonstrated that the vertical easterly wind shear plays a crucial role in inducing baroclinic vorticity ahead of northward
228   propagation of summer intra-seasonal oscillation. In order to find out the model forecast skill in predicting realistic easterly
229   wind shear (difference between zonal wind at 200 and 850 hPa) during summer monsoon season of 2022, the vertical wind
230   shear calculated and represented in Fig. 7a and 7b for GFS T1534 and HGFM respectively over the ISM region. Figure 7a
231   indicates slightly weaker easterly shear in GFS T1534 compared to ERA5 around 10°N and 0°-15°S for all lead times. On
232   the contrary, the HGFM is able to predict more realistic easterly wind shear over above regions as shown in the Fig. 7b. It is
233   noticeable that both models overestimate the magnitude of easterly shear around 20°N for Day-3 and Day-5 lead times.

234   Another key feature about tropical precipitation is almost equipartition of rainfall into convective and stratiform rain.
235   Therefore, it is important to investigate whether the relative improvement in the precipitation distribution over the ISM
236   region in HGFM forecasts is contributed by improved convective and large-scale precipitation. The model forecasted
237   convective and large-scale rainfall ratios are shown in Fig. 7c and 7d respectively. It is noteworthy that the large-scale or
238   stratiform rainfall plays an important role in the propagation and maintenance of the tropical intraseasonal convection
239   associated with its top-heavy heating profile (Fu and Wang, 2004; Chattopadhyay et al., 2009; Deng et al., 2015). The
240   heating profile associated with stratiform rain also helps in large-scale organization of convection (see for example,
241   Choudhary and Krishnan, 2011, Kumar et al., 2017). The contribution of convective rainfall to the total rainfall appears to be
242   more than 80 % in GFS T1534 forecast for all lead times (Fig. 7c). Similar overestimation of convective rainfall in GFS
243   T1534 is reported by Ganai et al. (2021). The observed convective (large-scale) rainfall ratio is around 55 % (45 %) as
244   shown in Abhik et al. (2017). The HGFM forecast shows relative improvement in predicting convective and large-scale
245   rainfall ratio compared to GFS T1534 (Fig. 7c and 7d). The decrease (increase) in convective (large-scale) rainfall
246   contribution to total rain is noted in HGFM forecast. The finer horizontal resolution in HGFM possibly allows for a more
247   accurate representation of deep convective due to scale-aware representation.
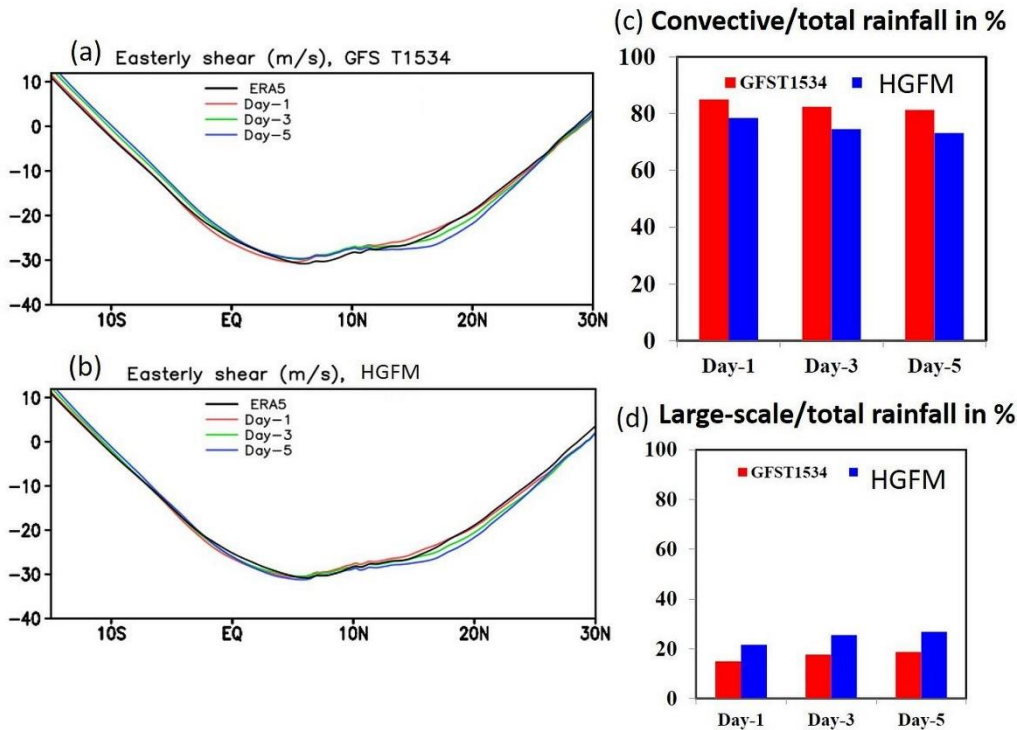
Figure 7. Comparison of easterly shear (m/s) from ERA-5 with GFS T1534 (a) and HGFM (b) along with convective/total rainfall (c) and large scale/total rainfall (d) between GFS T1534 and HGFM during JJAS 2022 for day-1 day-3 and day-5 lead time.

To attain further clarity about the model precipitation and moist convective processes, the vertical profile of relative humidity as a function of rain rate is analyzed for JJAS of 2022 over the ISM region (60°E-100°E, 10°S-30°N). The bias analysis suggests that GFS T1534 has systematically underestimated the lower-level moisture for all lead times (Fig. 8b). It is consistent with the study by Mukhopadhyay et al. (2019) and Ganai et al. (2021) where they reported similar underestimation of lower-level moisture over the ISM region IN GFS T1534 forecast. In contrast, the HGFM shows relative improvement in the lower-level moisture distribution, as depicted in Fig. 4c for all lead times. The enhancement of the lower-level moisture is visible as compared to GFS T1534 forecast. However, the upper troposphere is too moist for both model forecasts and need further improvement.

It is observed that overall statistics of monsoon rainfall and related convective processes have significantly improved in the HGFM model. In the next section some recent tropical cyclone forecasts are analysed.

261
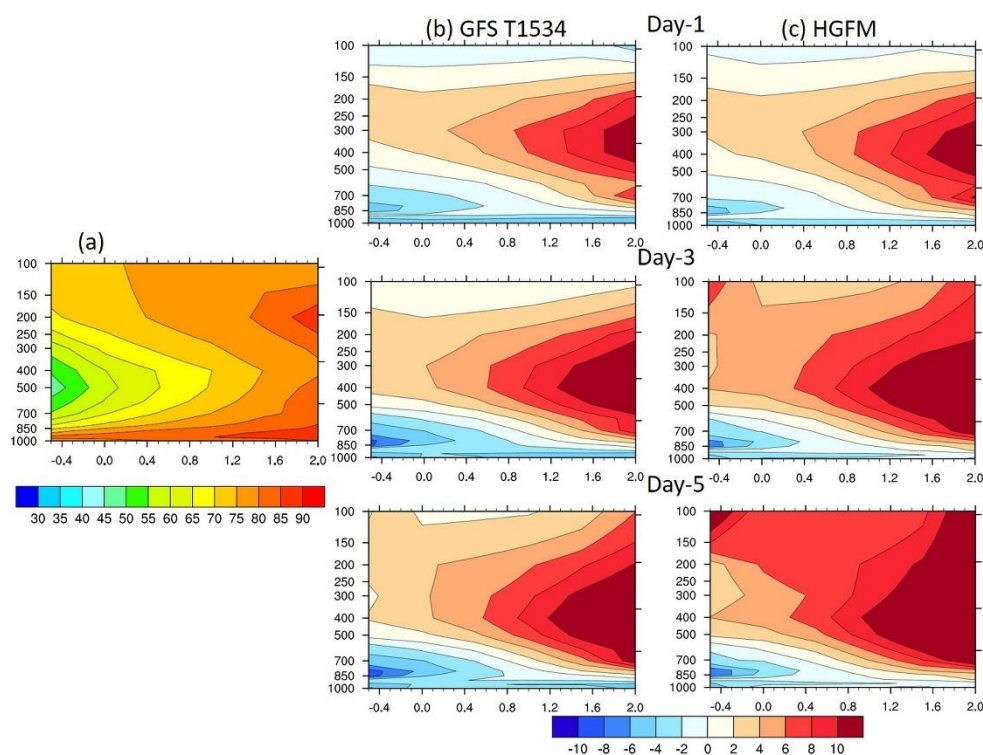
Figure 8. Comparison of Relative humidity (%, bias in shaded) vs rain rate (mm/day) over ISM region (60° E-100° E, 10° S-30° N) during JJAS-2022 from ERA-5 and IMERG (a) with GFS T1534 (b) and HGFM (c) during JJAS 2022 for day-1 day-3 and day-5 lead time.

3.5 Evaluation of Heavy Rainfall event

A very heavy rainfall event occurred on 22 August 2022 over central India. This event was well captured by both GFS and HGFM models as compared to the observed rain from IMD-GPM (shown in Fig. 9). Both HGFM (Fig. 9a, b, c) and GFS T1534 (Fig. 9d, e, f) models simulated the heavy rainfall signature compared to IMD GPM (Fig. 9g) on day 1 and day 3 forecast. However, a major difference was noted for rainfall intensity and spatial distribution on longer lead time (day 5) in HGFM and GFS T1534. There is an underestimation of rainfall in both the models compared to observations. Whereas the HGFM captures the signal of the occurrence of heavy rainfall even at day 5 lead, which is almost negligible in GFS forecast.
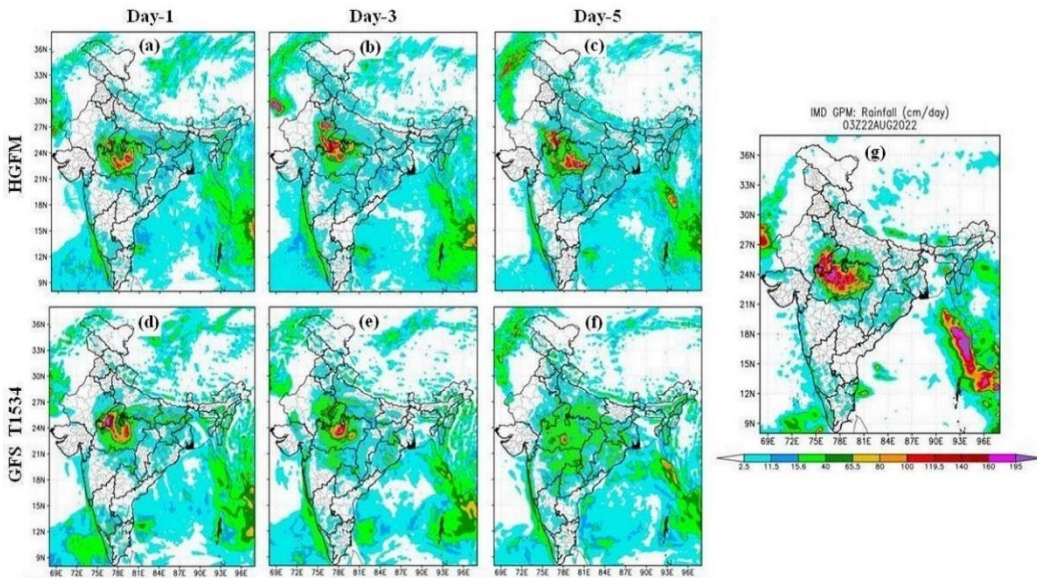
13

Figure 9. Comparison of heavy rainfall event on 22 August 2022 with HGFM (a, b, c), GFS T1534 (d, e, f) for day-1, day-3 and day-5 lead times with IMD GPM (g) rainfall.

3.5 Evaluation of Tropical Cyclone forecast

Total eight cases of tropical cyclones from 2022 and 2023 (RSMC 2022, RSMC 2023) are considered in the present study. Out of these 8 cases, 2 cyclones formed over the Arabian Sea and 6 cyclones over the Bay of Bengal (BOB). The observational data of track, intensity and landfall is obtained from IMD and referred as observations henceforth in the text. Figure 10 shows observed tracks (Fig. 10a) and observed intensity in terms of Maximum Sustained Wind Speed (MSW Fig. 10b) of the cyclones. The cyclones in the present study have different tracks and various range of severity in terms of intensity over both the basins.
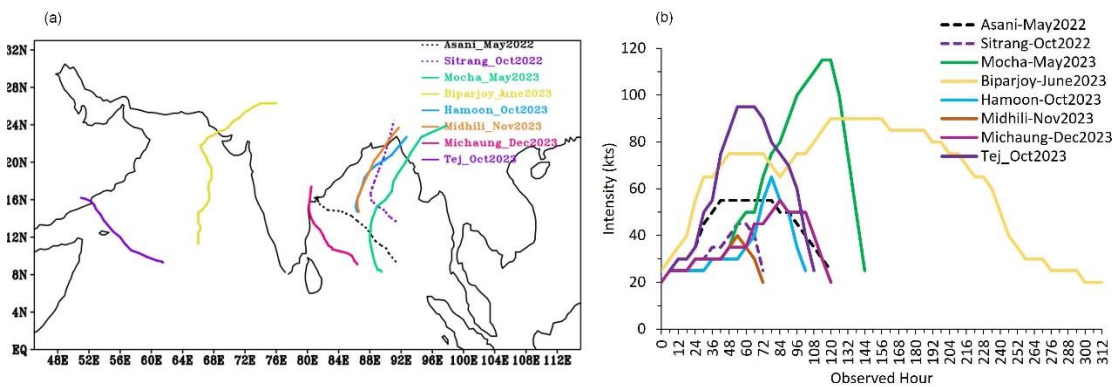
Figure 10. a) Observed tracks of the cyclones b) Observed Intensity in terms of Maximum Sustained Wind Speed (kts) during year 2022-2023.

14

Geoscientific
Model Development
Discussions

EGU

3.5.1 Annual Verification of GFS T1534 and HGFM Forecast for the year 2022 and 2023

For each cyclone case, the verification started from the observed Depression stage till observed landfall. For each cyclone case minimum four (maximum 10) initial conditions are considered as both the models have daily outputs. The errors calculated here are the average of all such samples for the year 2022 and 2023.

The Root Mean Square Error (RMSE) of track and intensity is shown in Fig. 11a-b. Initially upto 4 days, GFS T1534 and HGFM performs equally well but the considerable improvement with HGFM is noted after 4 days in both track and intensity forecast. Figure 11c-d   depicts the average track error and average intensity errors for all the cyclones. The average track errors as well as average intensity errors are reduced drastically in HGFM with longer lead hours (4 days or more). Average track errors (average intensity errors) are ~300 km (~20 kts) with 7 days leads in HGFM. The average landfall errors (both position and time) are also evaluated with IMD observations and are shown in Fig. 12. With 4days lead, average landfall position errors are ~200 km in HGFM and it reduces further with longer lead. In GFS T1534, landfall position errors are increasing with longer lead (compared to HGFM). Remarkable improvements are seen in the average landfall time errors in HGFM throughout the life cycle of cyclones. Overall, the track and intensity forecast are improved with HGFM for longer lead hours (~4 days or more), which is an added advantage for the early warning and mitigation purpose. Here, one of the cyclone cases (cyclone Biparjoy) is discussed in detail.
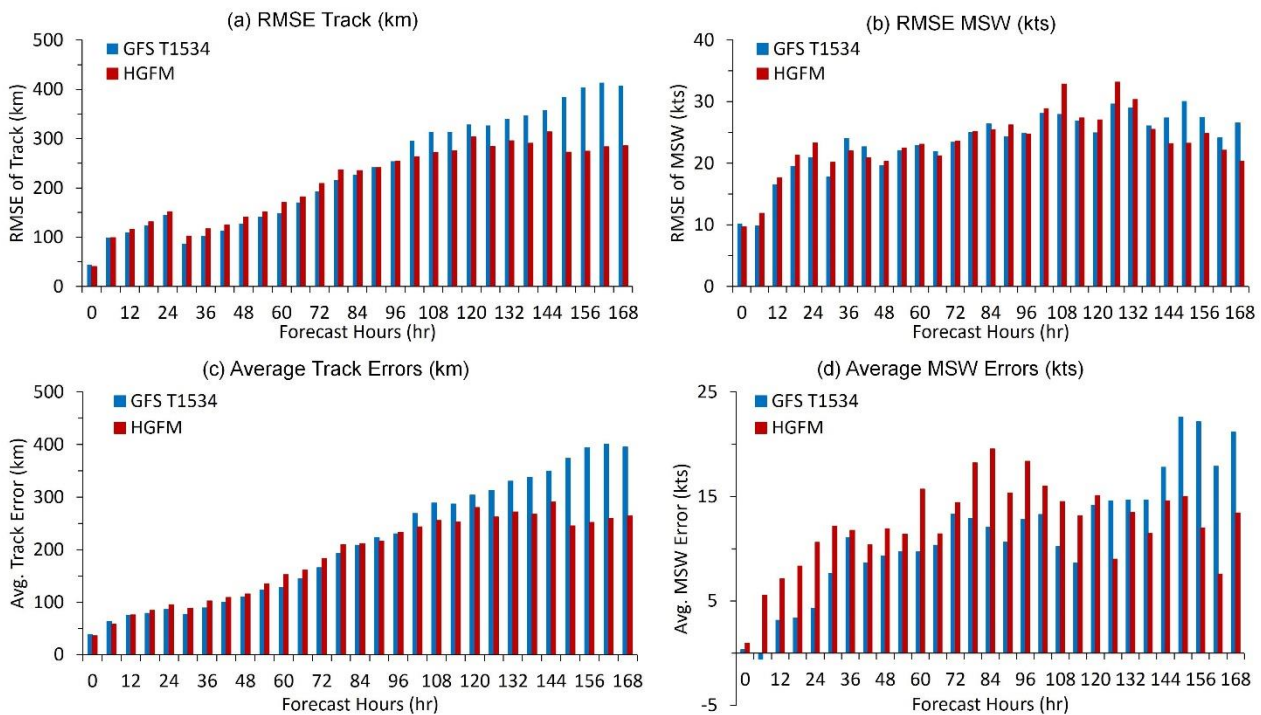
Figure 11. a) RMSE of Track in km b) RMSE of MSW in kts c) Average Track error (km) d) Average Intensity Errors (kts).

Geoscientific
Model Development
Discussions

302
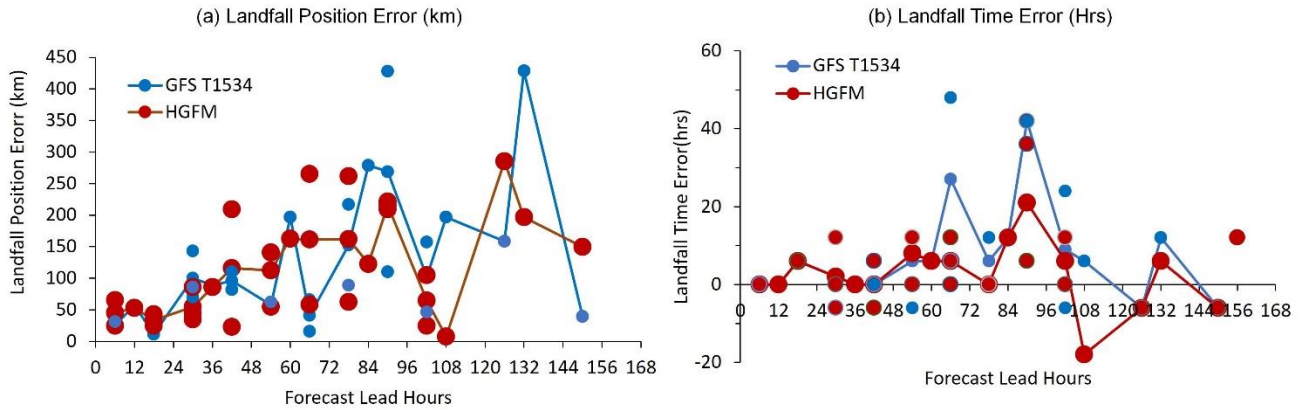
Figure 12. a) Average Landfall position errors in km b) Average Landfall time Errors in hours. The continuous lines represent the average errors for GFS T1534 (Blue) and HGFM (Red). The different size of the dots is for making the overlapped points visible.

3.5.2 A case study - Cyclone Biparjoy

During the monsoon onset of 2023 season, tropical cyclone Biparjoy evolved in the Arabian Sea and hit the north-western state of Gujarat, India. The cyclone Biparjoy lasted for quite a long time during 6-19 June 2023. It moved almost parallel to the Indian west coast and finally made landfall over the northern part of Gujarat and adjoining Pakistan. It has rapid intensification during its life cycle. The observed track shown in Fig. 13 as provided by IMD.

310
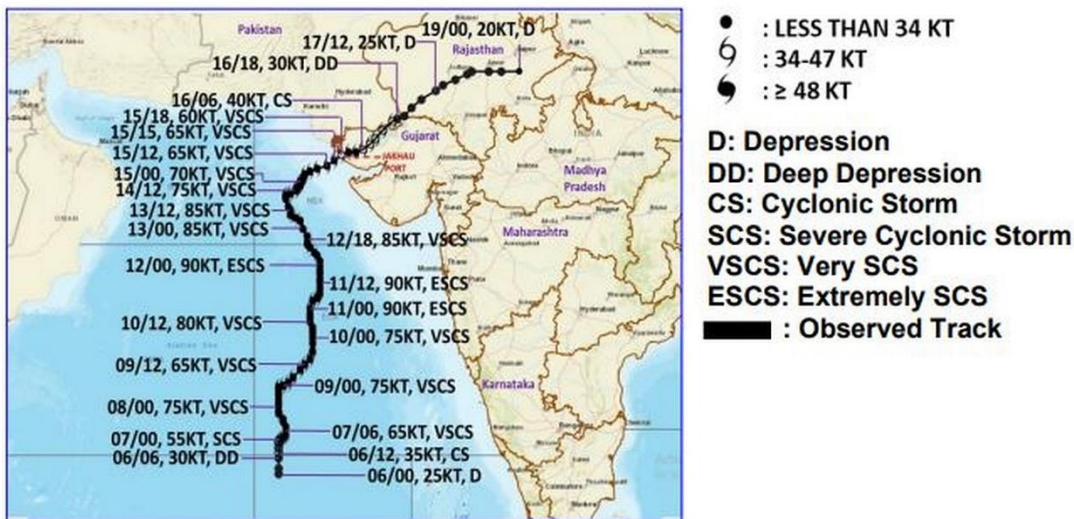
Figure 13. Observed track of Tropical cyclone Biparjoy over Arabian Sea during 6-19 June 2023 as per India Meteorological Department. Taken from open source: https://rsmcnewdelhi.imd.gov.in/report.php?internal_menu=Mjc= , page no. 90

16

Geoscientific
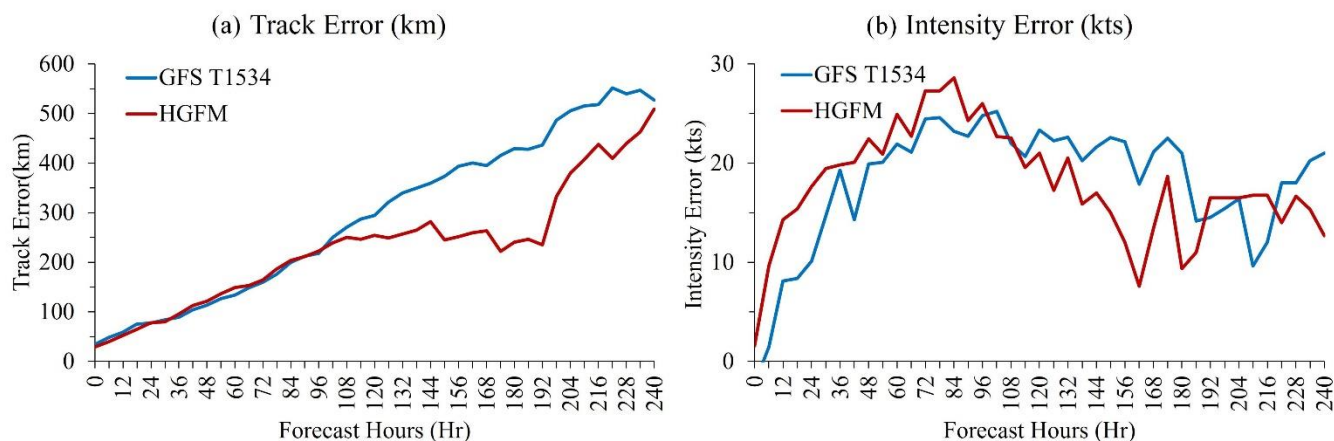Model Development
Discussions

313   The HGFM and GFS T1534 track forecast of TC Biparjoy based on 6 June initial condition, is shown in Fig. 14. It is evident

314   that the HGFM generates a track much closer to the observation as compared to GFS T1534. The intensity expressed in

315   terms of maximum sustained wind has been computed and shown in Fig. 13 for 10 days (240 forecast hours). The intensity

316   of the TC appears to be overestimated by both the models till 120 hrs of forecast and thereafter the intensity seems to be

317   reasonably predicted with 6 June 0000 UTC initial condition. Both the models are tested with different initial conditions

318   (from 6 June 00UTC to 15 June 00UTC, every 24 hrs). A comparative analysis of landfall position and landfall time errors

319   with HGFM and GFS T1534 with respect to the observations obtained from IMD has been mentioned in Table 2. It is

320   evident that the landfall position error of the cyclone has been significantly improved by HGFM forecast though the landfall

321   time error appears to be almost equivalent as compared to GFS T1534. Further the average track and intensity error

322   (obtained from 10 initial conditions) is depicted in Fig. 14a and 14b. It is evident that the HGFM produces more accurate

323   prediction of track with lesser error on longer lead while the errors are equivalent in the smaller lead.

324   **Table 2. Landfall position (km) and landfall time (hr) errors for the forecasts started with different initial conditions. -ve (+ve)**
325   **sign indicates early (late) landfall with respect to observed landfall time. The bold numbers indicates the significant improvement**
326   **in the landfall position errors with HGFM.**

Forecast Hours from Observed landfall (Hr)	Initial Condition	Landfall Position Error (km)		Landfall Time Error (Hr)	
		GFS T1534	HGFM	GFS T1534	HGFM
228	2023060600	298	**57**	0	-30
204	2023060700	No Landfall			
180	2023060800	616	**201**	0	0
156	2023060900	349	**197**	12	12
132	2023061000	428	**197**	12	6
108	2023061100	197	**7**	6	-18
84	2023061200	279	**123**	12	12
60	2023061300	197	**163**	6	6
36	2023061400	89	**86**	0	0
12	2023061500	57	**53**	0	0

345

Figure 14. a) Average track error and b) average intensity error for the tropical cyclone Biparjoy over Arabian Sea.

4 Conclusions

For the first time, a version of the GFS model utilizing a new grid structure triangular cubic octahedral (Tco) has been developed and is being run on an experimental basis for short to medium range weather prediction over the Indian region, designated as IITM High resolution Global Forecast Model (HGFM). The Tco grid provides a higher resolution over the tropics, making the model achieve 6.5 km horizontal resolution near the tropics. This higher resolution represents a substantial leap from the existing Gaussian linear GFS T1534 which maintains a resolution of 12.5 km across the globe. The KE spectra of 200 hPa zonal wind have also revealed reasonable power by both the model with HGFM showing marginally better power in the Kolmogorov region indicating fidelity of model structure.

The HGFM being developed in the Tco grid provides many advantages, notably resolving the Gibbs phenomenon and spurious rain over mountainous regions has been resolved. The June-September monsoon rainfall and a case study of heavy rainfall have been analyzed in detail. The newly developed HGFM shows significantly better skill, particularly in the longer lead and for heavier rain categories. Rainfall biases over the whole globe appear to be broadly similar between HGFM and GFS T1534. A case of heavier rainfall in and around central India during the monsoon season has been analysed where the validation shows a significant gain in forecast lead time by the HGFM compared to GFS T1534. The HGFM captures rainfall signature at 5 days lead time, when there is hardly any indication in the HGFM model forecast.

Several cases of tropical cyclones during 2022 and 2023 were analysed, indicating better performance of HGFM compared to GFS in predicting tracks and intensity. A case of tropical cyclone Biparjoy has been evaluated in detail based on IMD observation. It is seen that the HGFM model generates better accuracy of cyclone position in almost all lead time (Table 2) and further the average track error also is found to be much lesser as compared to GFS T1534 in longer lead. However, the errors of both model in average track and intensity are found to be equivalent.

368 This paper highlights the initial results of the newly developed HGFM model and its skill as compared to the operational
369 GFS T1534 model. Subsequently more analyses for many events will be carried out and the model will be made operational
370 for weather forecasts over India. The current set up of the model uses the same physics as the GFS model. However, the
371 HGFM model would require some parameter tuning to optimize the performance of the model and increase its fidelity. The
372 future work will be focused on detailed validation of model simulations with optimal set of physical parameterizations.
373
374
375
376
377
378

379 **Code and Data Availability**

380 The model simulated data used for HGFM and GFS T1534 in the study are available at "TCO model data" by R Phani
381 Murali Krishna, Kumar Siddharth, Athipatta Gopinathan Prajeesh, Malay Ganai, Revanth Reddy, Kumar Roy and
382 Parthasarathi Mukhopadhyay, DOI: https://doi.org/10.5281/zenodo.12569807. The model code is available at "GFS TCO
383 Model code" by R Phani Murali Krishna, Kumar Siddharth, Athipatta Gopinathan Prajeesh, Parthasarathi Mukhopadhyay.
384 DOI: https://doi.org/10.5281/zenodo.12526400
385

386 **Author Contributions**

387 RPMK, SK, AGP and PM conceptualised the problem and made necessary changes/modification development of code for
388 Tco and wrote the major part of the Introduction, data, methodology and over all sequences. PB and NW helped during
389 formulation of the Tco grid in GFS and helped in improving the manuscript writing. KR, MG, ST and TG made all the
390 forecast analysis of monsoon parameters and wrote the respective portion on analyses. RK made the analysis related to
391 cyclone forecast by HGFM model and wrote the section on the cyclone forecast analysis and BRR made the dCAPE analysis
392 and extracted the post processed variables for the analysis.
393
394

Competing interests

The authors declare that they have no conflict of interest.

Disclaimer

Acknowledgments

References

425 **References**

426 Abhik, S., Halder, M., Mukhopadhyay, P., Jiang, X., and Goswami, B.N.: A possible new mechanism for northward

427 propagation of boreal summer intraseasonal oscillations based on TRMM and MERRA reanalysis, Clim. Dyn., 40, 1611-

428 1624, https://doi.org/10.1007/s00382-012-1425-x, 2013.

429 Abhik, S., Krishna, R.P.M., Mahakur, M., Ganai, M., Mukhopadhyay, P., and Dudhia, J.: Revised cloud processes to

430 improve the mean and intraseasonal variability of Indian summer monsoon in climate forecast system: Part 1, J. Adv.

431 Model. Earth. Syst., 9(2), 1002-1029, https://doi.org/10.1002/2016MS000819, 2017.

432 Alpert, J.C., Kanamitsu, M., Caplan, P.M., Sela, J.G., White, G.H., and Kalnay, E.: Mountain induced gravity wave drag

433 parameterization in the NMC medium-range forecast model. In Conference on Numerical Weather Prediction, Baltimore,

434 MD, 8th, 726-733, 1988.

435 Arakawa, A. and Schubert, W.H.: Interaction of a cumulus cloud ensemble with the large-scale environment, Part I, J.

436 Atmos. Sci., 31(3), 674-701, https://doi.org/10.1175/1520-0469(1974)031<0674:IOACCE>2.0.CO;2, 1974.

437 Arakawa, A. and Wu, C.M.: A unified representation of deep moist convection in numerical modeling of the atmosphere.

438 Part I, J. Atmos. Sci., 70(7), 1977-1992, https://doi.org/10.1175/JAS-D-12-0330.1, 2013.

439 Bechtold, P., Köhler, M., Jung, T., Doblas-Reyes, F., Leutbecher, M., Rodwell, M. J., Vitart, F., and Balsamo, G.: Advances

440 in simulating atmospheric variability with the ECMWF model: From synoptic to decadal time-scales, Q. J. Roy. Meteor.

441 Soc., 134, 1337–1351, https://doi.org/10.1002/qj.289, 2008.

442 Chattopadhyay, R., Goswami, B.N., Sahai, A.K., and Fraedrich, K.: Role of stratiform rainfall in modifying the northward

443 propagation of monsoon intraseasonal oscillation, J. Geophys. Res. Atmos., 114(D19),

444 https://doi.org/10.1029/2009JD011869, 2009.

445 Choudhury, A.D. and Krishnan, R.: Dynamical response of the South Asian monsoon trough to latent heating from

446 stratiform and convective precipitation, J. Atmos. Sci., 68(6), 1347-1363, https://doi.org/10.1175/2011JAS3705.1, 2011.

447 Chun, H.Y. and Baik, J.J.: Momentum flux by thermally induced internal gravity waves and its approximation for large-scale

448 models, J. Atmos. Sci., 55(21), 3299-3310, https://doi.org/10.1175/1520-0469(1998)055<3299:MFBTII>2.0.CO;2, 1998.

449 Clough, S.A., Shephard, M.W., Mlawer, E.J., Delamere, J.S., Iacono, M.J., Cady-Pereira, K., Boukabara, S., and Brown,

450 P.D.: Atmospheric radiative transfer modeling: A summary of the AER codes, J. Quant. Spectrosc. Radiat. Transf., 91(2),

451 233-244, https://doi.org/10.1016/j.jqsrt.2004.05.058, 2005.

452 Crueger, T., Giorgetta, M.A., Brokopf, R., Esch, M., Fiedler, S., Hohenegger, C., Kornblueh, L., Mauritsen, T., Nam, C.,
453 Naumann, A.K., and Peters, K.: ICON-A, the atmosphere component of the ICON earth system model: II. Model evaluation,
454 J. Adv. Model. Earth. Syst., 10(7), 1638-1662, https://doi.org/10.1029/2017MS001233, 2018.

455 Deng, Q., Khouider, B., and Majda, A.J.: The MJO in a coarse-resolution GCM with a stochastic multicloud
456 parameterization, J. Atmos. Sci., 72(1), 55-74. https://doi.org/10.1175/JAS-D-14-0120.1, 2015.

457 Deshpande, M., Kanase, R., Krishna, R.P.M., Tirkey, S., Mukhopadhyay, P., Prasad, V.S., Johny, C.J., Durai, V.R., Devi, S.
458 and Mohapatra, M.: Global Ensemble Forecast System (GEFS T1534) evaluation for tropical cyclone prediction over the
459 North Indian Ocean, Mausam., 72(1), 119-128, https://doi.org/10.54302/mausam.v72i1.123, 2021.

460 ECMWF IFS DOCUMENTATION—Cy43r1 Operational Implementation Part IV: Physical Processes; ECMWF: Reading,
461 UK, 2016.

462 Fu, X. and Wang, B.: The boreal-summer intraseasonal oscillations simulated in a hybrid coupled atmosphere–ocean
463 model, Mon. Weather. Rev., 132(11), 2628-2649, https://doi.org/10.1175/MWR2811.1, 2004.

464 Gadgil, S. and Gadgil, S.: The Indian monsoon, GDP and agriculture, Econ. polit. Wkly., 4887-4895,
465 https://www.jstor.org/stable/4418949, 2006.

466 Ganai, M., Tirkey, S., Krishna, R.P.M., and Mukhopadhyay, P.: The impact of modified rate of precipitation conversion
467 parameter in the convective parameterization scheme of operational weather forecast model (GFS T1534) over Indian
468 summer monsoon region, Atmos. Res., 248, 105185, https://doi.org/10.1016/j.atmosres.2020.105185, 2021.

469 Giorgetta, M.A., Brokopf, R., Crueger, T., Esch, M., Fiedler, S., Helmert, J., Hohenegger, C., Kornblueh, L., Köhler, M.,
470 Manzini, E., and Mauritsen, T.: ICON-A, the atmosphere component of the ICON earth system model: I. Model description,
471 J. Adv. Model. Earth. Syst., 10(7), 1613-1637, https://doi.org/10.1029/2017MS001242, 2018.

472 Han, J. and Pan, H.L.: Revision of convection and vertical diffusion schemes in the NCEP Global Forecast System, Weather.
473 Forecast., 26(4), 520-533, https://doi.org/10.1175/WAF-D-10-05038.1, 2011.

474 Han, J., Witek, M.L., Teixeira, J., Sun, R., Pan, H.L., Fletcher, J.K., and Bretherton, C.S.: Implementation in the NCEP GFS
475 of a hybrid eddy-diffusivity mass-flux (EDMF) boundary layer parameterization with dissipative heating and modified stable
476 boundary layer mixing, Weather. Forecast., 31(1), 341-352, https://doi.org/10.1175/WAF-D-15-0053.1, 2016.

477 Han, J., Wang, W., Kwon, Y.C., Hong, S.Y., Tallapragada, V., and Yang, F.: Updates in the NCEP GFS cumulus convection
478 schemes with scale and aerosol awareness, Weather. Forecast., 32(5), 2005-2017, https://doi.org/10.1175/WAF-D-17-
479 0046.1, 2017.

480 Held, I.M. and Suarez, M.J.: A proposal for the intercomparison of the dynamical cores of atmospheric general circulation
481 models, Bull. Am. Meteorol. Soc., 75(10), 1825-1830, https://doi.org/10.1175/1520-
482 0477(1994)075<1825:APFTIO>2.0.CO;2, 1994.

483 Hersbach, H. and Dee, D.: ERA5 reanalysis is in production. ECMWF Newsletter No. 147,
484 ECMWF,Reading,UnitedKingdom,7, http://www.ecmwf.int/sites/default/files/elibrary/2016/16299-newsletter-no147-spring-
485 2016.pdf, 2016.

486 Hoffman, R.N., Kumar, V.K., Boukabara, S.A., Ide, K., Yang, F., and Atlas, R.: Progress in forecast skill at three leading
487 global operational NWP centers during 2015–17 as seen in summary assessment metrics (SAMs), Weather. Forecast., 33(6),
488 1661-1679, https://doi.org/10.1175/WAF-D-18-0117.1, 2018.

489 Huffman, G.J., Stocker, E.F., Bolvin, D.T., Nelkin, E.J., and Tan, J.: GPM IMERG Final Precipitation L3 Half Hourly 0.1
490 degree x 0.1 degree V06, Greenbelt, MD, Goddard Earth Sciences Data and Information Services Center (GES DISC),
491 Accessed: 20 March 2023, doi:10.5067/GPM/IMERG/3B-HH/06, 2019.

492 Iacono, M.J., Mlawer, E.J., Clough, S.A., and Morcrette, J.J.: Impact of an improved longwave radiation model, RRTM, on
493 the energy budget and thermodynamic properties of the NCAR community climate model, CCM3, J. Geophys. Res. Atmos.,
494 105(D11), 14873-14890, https://doi.org/10.1029/2000JD900091, 2000.

495 Jiang, X., Li, T., and Wang, B.: Structures and mechanisms of the northward propagating boreal summer intraseasonal
496 oscillation, J. Clim., 17(5), 1022-1039, https://doi.org/10.1175/1520-0442(2004)017<1022:SAMOTN>2.0.CO;2, 2004.

497 Kim, Y.J. and Arakawa, A.: Improvement of orographic gravity wave parameterization using a mesoscale gravity wave
498 model, J. Atmos. Sci., 52(11), 1875-1902, https://doi.org/10.1175/1520-0469(1995)052<1875:IOOGWP>2.0.CO;2, 1995.

499 Kinter, J.L., Cash, B., Achuthavarier, D., Adams, J., Altshuler, E., Dirmeyer, P., Doty, B., Huang, B., Jin, E.K., Marx, L.,
500 and Manganello, J.: Revolutionizing climate modeling with Project Athena: a multi-institutional, international collaboration,
501 Bull. Am. Meteorol. Soc., 94(2), 231-245, https://doi.org/10.1175/BAMS-D-11-00043.1, 2013.

502 Kumar, S., Arora, A., Chattopadhyay, R., Hazra, A., Rao, S.A., and Goswami, B.N.: Seminal role of stratiform clouds in
503 large-scale aggregation of tropical rain in boreal summer monsoon intraseasonal oscillations, Clim. Dyn., 48, 999-1015,
504 https://doi.org/10.1007/s00382-016-3124-5, 2017.

505 Kumar, S., Phani, R., Mukhopadhyay, P., and Balaji, C.: Does increasing horizontal resolution improve seasonal prediction
506 of Indian summer monsoon?: A climate forecast system model perspective, Geophys. Res. Lett., 49(7), e2021GL097466,
507 https://doi.org/10.1029/2021GL097466, 2022.

508 Lott, F. and Miller, M.J.: A new subgrid-scale orographic drag parametrization: Its formulation and testing, Q. J. R.
509 Meteorol. Soc., 123(537), 101-127, https://doi.org/10.1002/qj.49712353704, 1997.

510 Magnusson, L. and Källén, E.: Factors influencing skill improvements in the ECMWF forecasting system, Mon. Weather.
511 Rev., 141(9), 3142-3153, https://doi.org/10.1175/MWR-D-12-00318.1, 2013.

512 Mitra, A.K., Prakash, S., Imranali, M.M., Pai, D.S., and Srivastava, A.K.: Daily merged satellite gauge real-time rainfall
513 dataset for Indian Region, Vayumandal, 40(1–4), 33-43, 2014.

514 Miura, H., Satoh, M., Nasuno, T., Noda, A. T., and Oouchi, K.: A Madden-Julian Oscillation event realistically simulated by
515 a global cloud-resolving model, Sci., 318(5857), 1763–1765, https://doi.org/10.1126/science.1148443, 2007.

516 Molod, A., Takacs, L., Suarez, M., and Bacmeister, J.: Development of the GEOS-5 atmospheric general circulation model:
517 Evolution from MERRA to MERRA2, Geosci. Model. Dev., 8(5), 1339-1356, https://doi.org/10.5194/gmd-8-1339-205,
518 2015.

519 Mukhopadhyay, P., Prasad, V.S., Krishna, R.P.M., Deshpande, M., Ganai, M., Tirkey, S., Sarkar, S., Goswami, T., Johny,
520 C.J., Roy, K., and Mahakur, M.: Performance of a very high-resolution global forecast system model (GFS T1534) at 12.5
521 km over the Indian region during the 2016–2017 monsoon seasons, J. Earth Sys. Sci., 128, 1-18,
522 https://doi.org/10.1007/s12040-019-1186-6, 2019.

523 Mukhopadhyay, P., Bechtold, P., Zhu, Y., Murali Krishna, R.P., Kumar, S., Ganai, M., Tirkey, S., Goswami, T., Mahakur,
524 M., Deshpande, M., and Prasad, V.S.: Unraveling the mechanism of extreme (more than 30 sigma) precipitation during
525 August 2018 and 2019 over Kerala, India, Weather. Forecast., 36(4), 1253-1273, https://doi.org/10.1175/WAF-D-20-0162.1,
526 2021.

24

527   Nastrom, G.D. and Gage, K.S.: A climatology of atmospheric wavenumber spectra of wind and temperature observed by
528   commercial aircraft, J. Atmos. Sci., 42, 950–960, https://doi.org/10.1175/1520-0469(1985)042<0950:ACOAWS>2.0.CO;2,
529   1985.

530   Pan, H.L. and Wu, W.S.: Implementing a mass flux convection parameterization package for the NMC medium-range
531   forecast model. https://repository.library.noaa.gov/view/noaa/11429, 1995.

532   Prakash, S., Mitra, A.K., Momin, I.M., Rajagopal, E.N., Milton, S.F., and Martin, G.M.: Skill of short-to medium-range
533   monsoon rainfall forecasts from two global models over India for hydro-meteorological applications, Meteorol. Appl., 23(4),
534   574-586, https://doi.org/10.1002/met.1579, 2016.

535   Prasad, V.S., Mohandas, S., Gupta, M.D., Rajagopal, E.N., and Dutta, S.K.: Implementation of upgraded global forecasting
536   systems (T382L64 and T574L64) at NCMRWF, In NCMRWF Technical Report, 1-72, 2011.

537   Prasad, V.S., Mohandas, S., Dutta, S.K., Gupta, M.D., Iyengar, G.R., Rajagopal, E.N., and Basu, S.: Improvements in
538   medium range weather forecasting system of India, J. Earth. Sys. Sci., 123, 247-258, https://doi.org/10.1007/s12040-014-
539   0404-5, 2014.

540   Prasad, V.S., Johny, C.J., Mali, P., Singh, S.K., and Rajagopal, E.N.: Global retrospective analysis using NGFS for the
541   period 2000–2011, Current Sci., 370-377, https://www.jstor.org/stable/24912364, 2017.

542   Rajendran, K., Kitoh, A., Mizuta, R., Sajani, S., and Nakazawa, T.: High-resolution simulation of mean convection and its
543   intraseasonal variability over the tropics in the MRI/JMA 20-km mesh AGCM, J. Clim., 21(15), 3722-3739,
544   https://doi.org/10.1175/2008JCLI1950.1, 2008.

545   Rao, S.A., Goswami, B.N., Sahai, A.K., Rajagopal, E.N., Mukhopadhyay, P., Rajeevan, M., Nayak, S., Rathore, L.S.,
546   Shenoi, S.S.C., Ramesh, K.J., and Nanjundiah, R.S.: Monsoon mission: a targeted activity to improve monsoon prediction
547   across scales, Bull. Am. Meteorol. Soc., 100(12), 2509-2532, https://doi.org/10.1175/BAMS-D-17-0330.1, 2019.

548   RSMC Report, Report on Cyclonic disturbances over North Indian Ocean during 2022, India Meteorological Department,
549   https://rsmcnewdelhi.imd.gov.in/report.php?internal_menu=Mjc=

550   RSMC Report, Report on Cyclonic disturbances over North Indian Ocean during 2023, India Meteorological Department,
551   https://rsmcnewdelhi.imd.gov.in/report.php?internal_menu=Mjc=

552   Satoh, M., Tomita, H., Miura, H., Iga, S., and Nasuno, T.: Development of a global cloud resolving model-a multi-scale
553   structure of tropical convections, J. Earth. Simul., 3, 11-19, 2005.

554 Satoh, M., Stevens, B., Judt, F., Khairoutdinov, M., Lin, S.J., Putman, W.M., and Düben, P.: Global cloud-resolving models,
555 Curr. Clim. Change Rep., 5, 172-184, https://doi.org/10.1007/s40641-019-00131-0, 2019.

556 Skamarock, W.C., Klemp, J.B., Duda, M.G., Fowler, L.D., Park, S.H., and Ringler, T.D.: A multiscale nonhydrostatic
557 atmospheric model using centroidal Voronoi tesselations and C-Grid staggering, Mon. Weather. Rev., 140(9), 3090–
558 3105, https://doi.org/10.1175/MWR-D-11-00215.1, 2012.

559 Stephens, G.L., L'Ecuyer, T., Forbes, R., Gettelmen, A., Golaz, J.C., Bodas-Salcedo, A., Suzuki, K., Gabriel, P., and Haynes,
560 J.: Dreary state of precipitation in global models, J. Geophys. Res. Atmos., 115(D24), https://doi.10.1029/2010JD014532,
561 2010.

562 Sundqvist, H., Berge, E., and Kristjánsson, J.E.: Condensation and cloud parameterization studies with a mesoscale
563 numerical weather prediction model, Mon. Weather. Rev., 117(8), 1641-1657, https://doi.org/10.1175/1520-
564 0493(1989)117<1641:CACPSW>2.0.CO;2, 1989.

565 Watson, P.A., Berner, J., Corti, S., Davini, P., von Hardenberg, J., Sanchez, C., Weisheimer, A., and Palmer, T.N.: The
566 impact of stochastic physics on tropical rainfall variability in global climate models on daily to weekly time scales, J.
567 Geophys. Res. Atmos., 122(11), 5738-5762, https://doi.org/10.1002/2016JD026386, 2017.

568 Wedi, N.P., Polichtchouk, I., Dueben, P., Anantharaj, V.G., Bauer, P., Boussetta, S., Browne, P., Deconinck, W., Gaudin,
569 W., Hadade, I., and Hatfield, S.: A baseline for global weather and climate simulations at 1 km resolution, J. Adv. Model.
570 Earth. Syst., 12(11), e2020MS002192, https://doi.org/10.1029/2020MS002192, 2020.

571 Westra, S., Fowler, H.J., Evans, J.P., Alexander, L.V., Berg, P., Johnson, F., Kendon, E.J., Lenderink, G., and Roberts, N.:
572 Future changes to the intensity and frequency of short-duration extreme rainfall, Rev. Geophys., 52(3), 522-555,
573 https://doi.10.1002/2014RG000464, 2014.

574 Zhang, G.J.: Convective quasi-equilibrium in the tropical western Pacific: Comparison with midlatitude continental
575 environment, J. Geophys. Res. Atmos., 108(D19), https://doi.org/10.1029/2003JD003520, 2003.

576 Zhao, Q. and Carr, F.H.: A prognostic cloud scheme for operational NWP models, Mon. Weather. Rev., 125(8), 1931-1953,
577 https://doi.org/10.1175/1520-0493(1997)125<1931:APCSFO>2.0.CO;2, 1997.